Melting relations and major element partitioning in an oxidized bulk Earth model composition at 15–26 GPa

Reidar G. Trønnes [*]

C.M. Scarfe Laboratory of Experimental Petrology, University of Alberta, Edmonton, Canada

Abstract

Melting experiments were performed on an FeO-rich bulk Earth model composition in the CMFAS system in order to investigate the partitioning of major elements between coexisting minerals and melts. The starting material (34.2% SiO_2, 3.86% Al_2O_3, 35.2% FeO, 25.0% MgO and 1.88% CaO), contained in Re-capsules, was a mixture of crystalline forsterite and fayalite, and a glass containing SiO_2, Al_2O_3, and CaO. Olivine is the first liquidus phase at 10 GPa but is replaced by majoritic garnet (ga) in the 15–26 GPa range. Magnesiowüstite (mw) crystallizes close to the liquidus and is joined by perovskite (pv) at 26 GPa.

The quenched melt compositions are homogeneous throughout the melt region of the charges and are only slightly enriched in Si, Ca and Fe, and depleted in Mg, relative to the starting composition. The Fe/Mg and Ca/Al ratios in all of the minerals increase rapidly below the liquidus to become compatible with the bulk composition at the solidus. At 26 GPa, a relative density sequence of mw > pv > melt > ga is observed. This indicates that majorite floating, combined with the sinking of magnesiowüstite and perovskite can be expected during the solidification of a Hadean magma ocean and in hot mantle plumes early in the Earth's history. The mineral–melt partitioning relations indicate that fractional crystallization or partial melting in the transition zone and the upper part of the lower mantle would increase the Fe/Mg and Ca/Al ratios of the melt, even if magnesiowüstite was predominant in the solid fraction. A significant contribution of accumulated mw to the segregation of the protocore is therefore unlikely. The suggested process of perovskite fractionation to the lower mantle is not capable of increasing the Mg/Si ratio in the residual melt, and the combined fractionation of perovskite and magnesiowüstite produces a melt with elevated ratios of Si/Mg, Ca/Al and Fe/Mg. © 2000 Elsevier Science B.V. All rights reserved.

Keywords: Bulk Earth model composition; Element partitioning; Magnesiowüstite; Melting relations; Perovskite

1. Introduction

Extensive melting of the terrestrial planets during accretion and core formation may have created deep magma oceans (Wetherill, 1990; Tonks and Melosh, 1993). Mineral–melt separation processes of uncertain and variable efficiency were probably operating during the solidification of a terrestrial magma ocean (Agee and Walker, 1988; Solomatov and Stevenson, 1993) and during more localized melting and crystallization in rising columns of hot mantle (Herzberg, 1995). A chemically stratified mantle is a possible outcome of efficient mineral–melt separation in the

[*] Present address: Nordic Volcanological Institute, University of Iceland, Grensasvegur 50, IS-108 Reykjavik, Iceland. Tel.: +354-525-4496; fax: +354-562-9767.
E-mail address: rgt@norvol.hi.is (R.G. Trønnes).

early Earth. Later in the Earth's history, the separation of melt from rising plumes of hot mantle may have contributed to chemical heterogeneities in the mantle.

Improved data on melting relations and mineral–melt partitioning is needed to increase our understanding of the consequences of melt–solid fractionation processes in the mantle. Melting studies on peridotitic mantle compositions in the 1–25 GPa pressure range have provided a considerable amount of information on the melting relations and mineral–melt partitioning in these systems, especially up to 10 GPa (e.g., O'Hara, 1968, Herzberg and O'Hara, 1998; Green, 1995; Jones, 1995). At 20–26 GPa, near the upper end of the attainable pressure range of the conventional multi-anvil apparatus, extreme thermal gradients cause problems in the evaluation of the liquidus phase relations and mineral–melt partitioning. Therefore, further melting studies in reasonably large pressure cells, where the thermal gradients are kept low, regular and stable, are needed. An investigation emphasizing the liquidus phase relations and mineral–melt partitioning between magnesiowüstite (mw), perovskite (pv) and majoritic garnet (ga) has been performed in an FeO-rich bulk Earth model composition in the CMFAS system (35% FeO). The choice of this composition was motivated by the importance of establishing the partitioning relations of major elements between these phases, also in systems that are more FeO-rich than common peridotites. Partitioning data for iron-rich compositions may be relevant to the very early stages of crystallization in deep magma oceans on terrestrial planets. Agee (1990, 1993) and Agee et al.

(1995) conducted melting experiments on the Allende meteorite, containing 27% FeO and 4% FeS, and found that magnesiowüstite and garnet crystallized at the liquidus in the 24–26 GPa pressure range. They suggested that magnesiowüstite fractionation to the lower mantle could be a viable precursor to core formation, especially if FeO has an enhanced affinity to enter the core alloy at extreme pressures and temperatures. The presence of magnesiowüstite as a near-liquidus phase even in peridotitic systems was documented by McFarlane et al. (1991) and Zhang and Herzberg (1994). The mineral–melt partitioning relations involving magnesiowüstite, garnet, and perovskite is, therefore, important for melt generation in the transition zone and the upper part of the lower mantle also during the later stages of the Earth's history.

2. Experimental and analytical procedures

The starting material was a mixture of crystalline forsterite and fayalite and a glass containing SiO_2, Al_2O_3, and CaO. The mixture was prepared as a CMFAS analogue of average CI chondritic composition (Anders and Grevesse, 1989). The composition of the mixed and homogenized material was measured directly on quenched melt produced in a supraliquidus experiment at 4 GPa (Tables 1 and 2). This composition, which was confirmed by XRF analysis on a powder split, differs slightly from the assumed starting material composition reported by Trønnes et al. (1992). The oxidized (all Fe as FeO)

Table 1
List of experiments

Run number	p (GPa)	Nominal T (°C)	Estimated liquid T (°C)	Duration (min)	Crystallization sequence
1329	4.0	1970		2	supraliquidus
1275	10.0	1850	1890	20	ol, mw
1337	14.8	1925	2000	20	ga, mw, ol
1257	19.8	2000	2110	12	ga, mw
1251	22.8	2250	2150	30	ga, mw
1273	24.3	2100	2165	10	ga, mw
1274	26.2	2120	2180	10	pv–mw–ga

Number 1329 was run in an 18-11 mm configuration in a graphite capsule and provided 100% quenched melt for bulk composition analyses. Number 1275 was run in a 14-8 mm configuration. pv, perovskite; ga, majoritic garnet; mw, magnesiowüstite.

Table 2
Chemical composition of starting material, quenched melts and coexisting minerals

	SiO_2	Al_2O_3	FeO	MgO	CaO	$\Sigma_{wt.\%}$	Si	Al	Fe	Mg	Ca	Σ_{cat}	Fe/Mg
Bulk composition	34.2	3.86	35.2	25.0	1.88	100.1	2.85	0.38	2.45	3.11	0.17	8.96	0.79
QM													
26.2 L	36.3	4.12	35.8	21.4	2.40	100.0	3.02	0.4	2.49	2.65	0.21	8.78	0.94
24.3 L	36.0	3.66	36.5	21.3	2.36	99.8	3.02	0.36	2.54	2.66	0.21	8.80	0.96
22.8 L	35.9	3.91	36.0	21.6	2.19	99.6	3.01	0.39	2.52	2.69	0.20	8.80	0.94
19.8 L	36.3	3.78	35.1	22.3	2.48	100.0	3.01	0.37	2.44	2.76	0.22	8.80	0.88
14.8 L	35.2	3.23	37.5	22.3	2.17	100.4	2.95	0.32	2.63	2.79	0.20	8.89	0.94
14.8 mw-in	33.9	2.64	40.0	21.7	2.02	100.3	2.90	0.27	2.86	2.76	0.18	8.97	1.03
pv													
26.2 L	51.1	5.27	13.0	29.7	0.60	99.7	3.67	0.45	0.78	3.18	0.05	8.11	0.25
26.2 interm	50.0	5.15	15.6	28.5	0.89	100.1	3.62	0.44	0.95	3.08	0.07	8.16	0.31
26.2 S	49.8	4.73	19.6	25.1	1.58	100.8	3.66	0.41	1.20	2.75	0.12	8.14	0.44
ga													
26.2 L	49.1	12.5	11.0	25.0	2.26	99.9	3.48	1.04	0.65	2.64	0.17	7.99	0.25
26.2 interm	47.8	12.1	14.5	20.7	4.24	99.3	3.49	1.04	0.88	2.25	0.33	7.99	0.39
26.2 S	48.1	9.8	17.5	18.5	5.65	99.6	3.57	0.86	1.09	2.05	0.45	8.00	0.53
24.3 L	50.1	10.9	10.8	25.9	2.16	99.9	3.55	0.91	0.64	2.73	0.16	8.00	0.23
22.8 L	49.7	12.2	9.76	26.4	1.72	99.8	3.50	1.01	0.58	2.77	0.13	7.99	0.21
19.8 L	48.8	14.0	9.78	25.5	1.82	99.9	3.43	1.16	0.58	2.68	0.14	7.98	0.22
14.8 L	48.2	14.3	11.6	24.6	1.40	100.1	3.41	1.19	0.69	2.60	0.11	7.99	0.26
mw													
26.2 L	0.32	1.28	53.6	45.0	0.07	100.3	0.03	0.16	4.68	7.01	0.01	11.9	0.67
26.2 interm	0.27	0.77	64.2	35.0	0.14	100.4	0.03	0.10	5.97	5.80	0.02	11.9	1.03
26.2 S	0.30	0.42	68.2	29.9	0.19	99.0	0.03	0.06	6.64	5.18	0.02	11.9	1.28
24.3 L	0.30	1.16	56.7	41.8	0.06	100.0	0.03	0.15	5.06	6.65	0.01	11.9	0.76
22.8 L	0.30	1.18	59.5	38.7	0.07	9.8	0.03	0.15	5.42	6.28	0.01	11.9	0.86
19.8 L	0.29	1.22	58.3	39.5	0.06	99.4	0.03	0.16	5.30	6.40	0.01	11.9	0.83
14.8 mw-in	0.58	0.76	64.6	33.6	0.05	99.6	0.07	0.10	6.08	5.63	0.01	11.9	1.08
Estimated 1σ													
QM	1.0	0.23	1.3	0.9	0.28								
pv, ga	0.9	0.19	0.5	0.7	0.16								
mw	0.03	0.05	1.2	1.0	0.02								

Oxides in weight percent, cations normalized to a total charge of 24 (12 oxygen atoms). The phase compositions are average values of 10–30 analyses. The bulk composition was measured on the quenched melt contained in a graphite capsule, run at 4 GPa and 1970°C (supraliquidus condition). The numbers 26.2, 24.3, 22.8, 19.8, and 14.8 denote pressure (in GPa), and correspond to experimental run numbers 1274, 1273, 1251, 1257, and 1337, respectively. QM, quenched melt; pv, perovskite; ga, majoritic garnet; mw, magnesiowüstite; L, near the liquidus interface; S, near solidus (700 μm below the liquidus); interm, intermediate between liquidus and solidus (350 μm below the liquidi; mw-in, interstitial melt or mw near the line of incoming mw.

CMFAS composition used in this study is intermediate between the correspondingly oxidized bulk Earth estimate of Allegre et al. (1995) and average C1 chondrite of Anders and Grevesse (1989) in four of the oxides and somewhat higher in alumina.

The experiments were conducted in the uni-axial split-sphere apparatus (MA 6-8) at the University of Alberta, using a 10/4-mm configuration. Fig. 1 gives the calibration curves and further description. Based on the recommended revision of the ilmenite–perovskite transition for $MgSiO_3$ by Kato et al. (1995) and the coesite–stishovite transition by Zhang et al. (1994), the pressure calibration used in this paper is slightly adjusted, relative to the calibration in the preliminary reports of Trønnes et al. (1992) and Trønnes (1998).

The heating was accomplished using $LaCrO_3$ furnaces, and the temperature was measured with axially inserted WRe_3–WRe_{25} thermocouples (Fig. 2). No correction was made for the pressure effect on
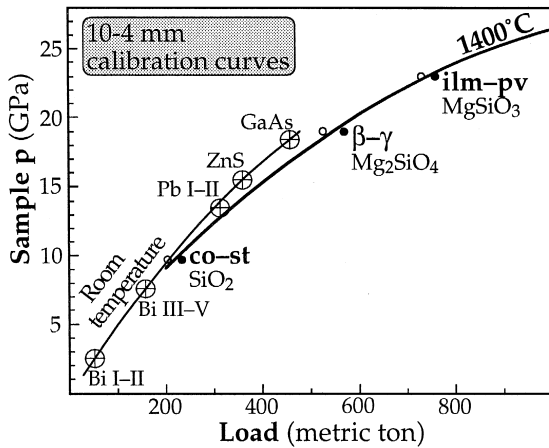
Fig. 1. Pressure calibration curves for 4-mm truncation edge lengths on 32-mm Toshiba F-grade WC with 10-mm octahedral pressure cells of MgO–5% Cr_2O_3 and 2.75-mm thick and 5.00-mm wide pyrophyllite gaskets. The calibration points at 1400°C are the transitions coesite–stishovite, wadsleyite–spinel (Mg_2SiO_4) and ilmenite–perovskite ($MgSiO_3$) at 9.7, 19.4, and 23.0 GPa, respectively.

the thermocouple EMF. The temperature was stable within ± 3–8°C during the 10- to 30-min long experiments. The thermal gradients along the furnace axis within the sample are estimated to be 180–250°C/mm. The rate of heating during the approach to run temperature was 60–80°C/min.

The samples were contained in Re capsules. No Fe-dominated metallic phase was formed during the experiments, but small amounts of Fe alloyed with Re near the inner walls of the sample capsules, especially in the melt portions of the capsules. The innermost Re walls and small Re protrusions into the melt portions contain a maximum of 1 wt.% Fe, but mostly less than 0.4 wt.% Fe. These findings are in accordance with Zhang and Herzberg (1994) and Herzberg and Zhang (1997), who found that the oxygen fugacity in similar assemblies with Re capsules and $LaCrO_3$ heaters is only slightly above the iron–wüstite buffer. Tiny grains of Re were produced during the cutting and preparation of the Re foil to capsules, and some of these grains became mixed with the sample powder during packing of the sample powder into the capsules. These 2- to 8-μm Re grains settled through the melt portion of the charges during the experiments and collected at the top of the lower liquidus interface. They were al-

loyed with up to 5 wt.% Fe and served as excellent top–bottom markers (Fig. 4).

The phases were analyzed by electron microprobe, partly at the University of Alberta, but mainly in the joint facility of IKU Petroleum Research and the Geological Survey of Norway in Trondheim. This facility is equipped with a Jeol 733X Superprobe with four wavelength-dispersive spectrometers. The instrument operated at an accelerating voltage of 15 kV with a beam current of 15 nA and counting time of 20 s on the peaks. The raw data were corrected by a Jeol ZAF program. Standards used were wollasonite for Ca and Si, kyanite for Al, and olivine for Mg and Fe. The mw was also analyzed with magnetite as an Fe standard. The minerals were analyzed partly with a focused and stationary beam, and partly with a raster mode of analysis covering areas of up to 10 μm². The raster areas used for analyses of quenched melts ranged from 400 to 700 μm². The estimated precision and accuracy for analyses of quenched melt and different minerals, given in Table 2, are based on repeated analyses of the experimental phases and standards (10–30 analyses of each phase). Although the spatial variation of quenched melt compositions within the all-melt portions of the experimental charges are
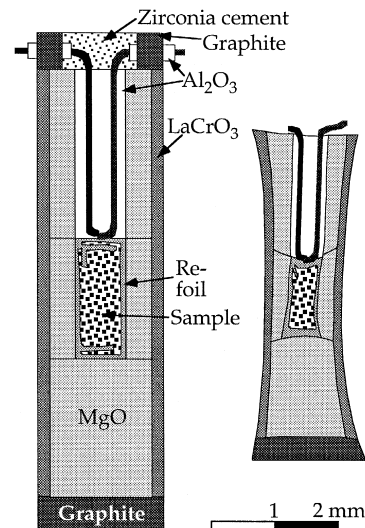

Fig. 2. Cross-sections through the furnace assembly (10/4 mm configuration) before (left) and after (right) the experiments in the 24–26 GPa range.

generally within the precision range, the reported melt analyses are from areas close to the liquidus. Some of the ga crystals between the liquidus and the solidus are slightly zoned. In these cases, the cores have higher Fe/Mg ratios of the rims, and they represent incompletely equilibrated subsolidus compositions formed during heating (60–80°C/min) toward the run temperature. In the case of zoned crystals, the spot analyses were performed on the rims in equilibrium with the adjacent melt.

3. Results

3.1. Melting relations

The approximate liquidus phase diagram of the FeO-rich bulk Earth model composition is shown in Fig. 3. The diagram is based on the variation in phase assemblage along the thermal gradient at isobaric sections at 10, 14.8, 19.8, 22.8, 24.3, and 26.2 GPa. The inferred subsolidus phase transitions are based on Agee et al. (1995). Olivine is the first liquidus phase at 10 GPa but is replaced by majorititic garnet at 12–14 GPa. Magnesiowüstite is the second phase to crystallize at all pressures from 10 to 25 GPa, and garnet persists as the first liquidus phase up to about 25 GPa. At 26.2 GPa, garnet and magnesiowüstite are joined by perovskite. The three
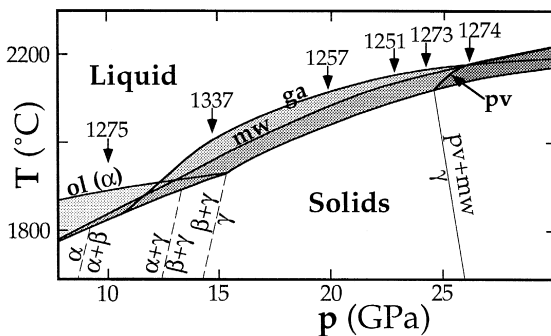

Fig. 3. Approximate phase diagram constructed from *T*-dependent variation of suprasolidus phase assemblages along isobaric sections. The experimental run numbers are shown at their respective pressures. Inferred subsolidus phase transitions are based on Agee et al. (1995). Metallic iron is not present and the Fe contents of the inner walls of the Re capsules are less than 1 wt.%. Tiny Re fragments immersed in the quenched melt contain up to 6 wt.% Fe. pv, perovskite; ga, majoritic garnet; mw, magnesiowüstite; α, olivine; β, wadsleyite; γ, ringwoodite.

phases appear to be nearly cotectic and it is difficult to judge the exact sequence of crystallization.

Fig. 4 shows back-scattered electron (BSE) images of the liquidus phase relations at 14.8 and 26.2 GPa. The thermal gradients are estimated to be 180–200°C/mm and 200–250°C/mm in the two experiments, respectively. In the 14.8 GPa experiment (Fig. 4A), a 250-μm wide zone of scattered garnet crystals and interstitial liquid occurs between the all-melt portion and a zone of garnet intergrown with magnesiowüstite. A $(MgFe)_2SiO_4$ phase joins the ga–mw assemblage near the cold end of the charge.

The 26.2 GPa experiment (Fig. 4B–E) demonstrates the differential density relations between melt, garnet, perovskite and magnesiowüstite, with a different development of the upper and lower liquidus interface. The lower liquidus boundary is marked by a fine string of tiny (2–8 mm) Re-fragments that settled through the melt portion of the charge. The two densest phases, perovskite and magnesiowüstite, are the dominant minerals along the lower liquidus interface. Along the upper liquidus interface, these two dense phases appear to have selectively settled into the hot melt zone and dissolved. More buoyant crystals of garnet therefore predominate along the liquidus interface. Based on these observations, a relative density sequence of mw > pv > melt > ga is inferred for such an FeO-rich composition at 26.2 GPa. The effect of differential buoyancy and dissolution/precipitation did not cause appreciable chemical inhomogenieties in the quenched melt during the 10-min long experiment.

3.2. Phase composition and major element partitioning

The quenched melt and mineral compositions are listed in Table 2, and Figs. 5 and 6 show the liquidus phase compositions at 19.8–24.3 GPa and liquidus to subsolidus phase compositions at 26.2 GPa. The quenched melt compositions are homogeneous throughout the melt-region of the charges within the analytical precision and are only slightly enriched in Si, Ca and Fe, and depleted in Mg, relative to the starting composition. The melt compositions in the 15–26 GPa range are rather similar and do not vary systematically with pressure. As demonstrated in
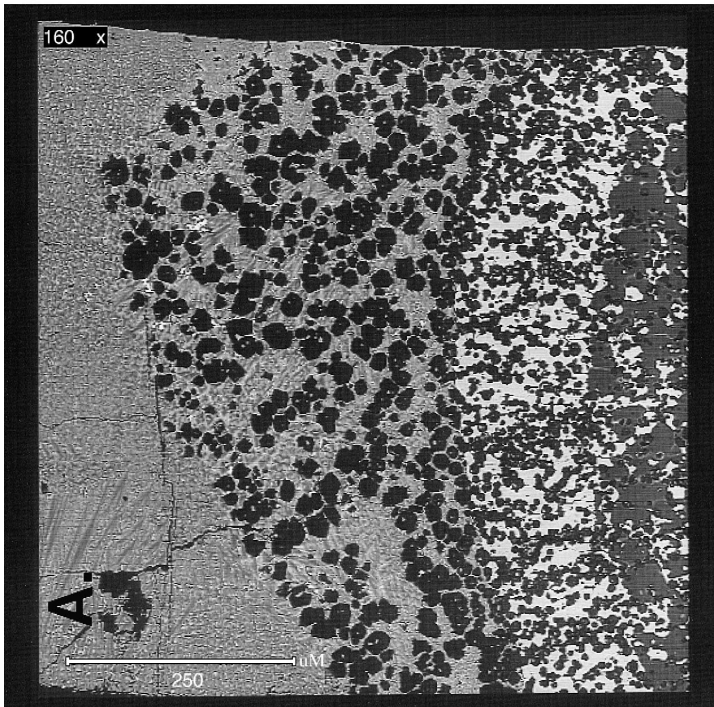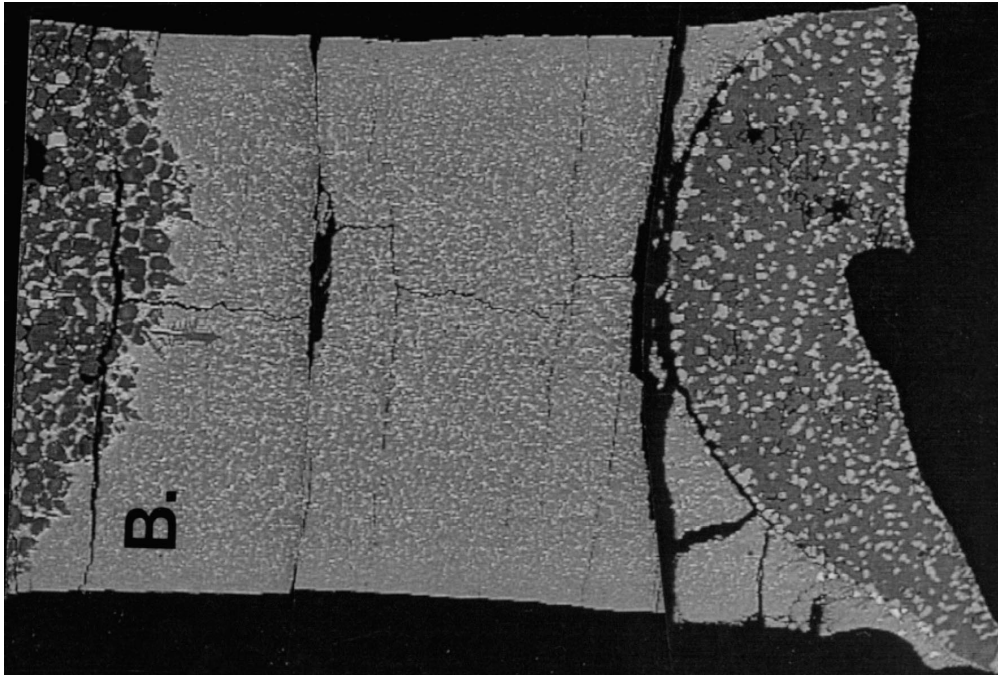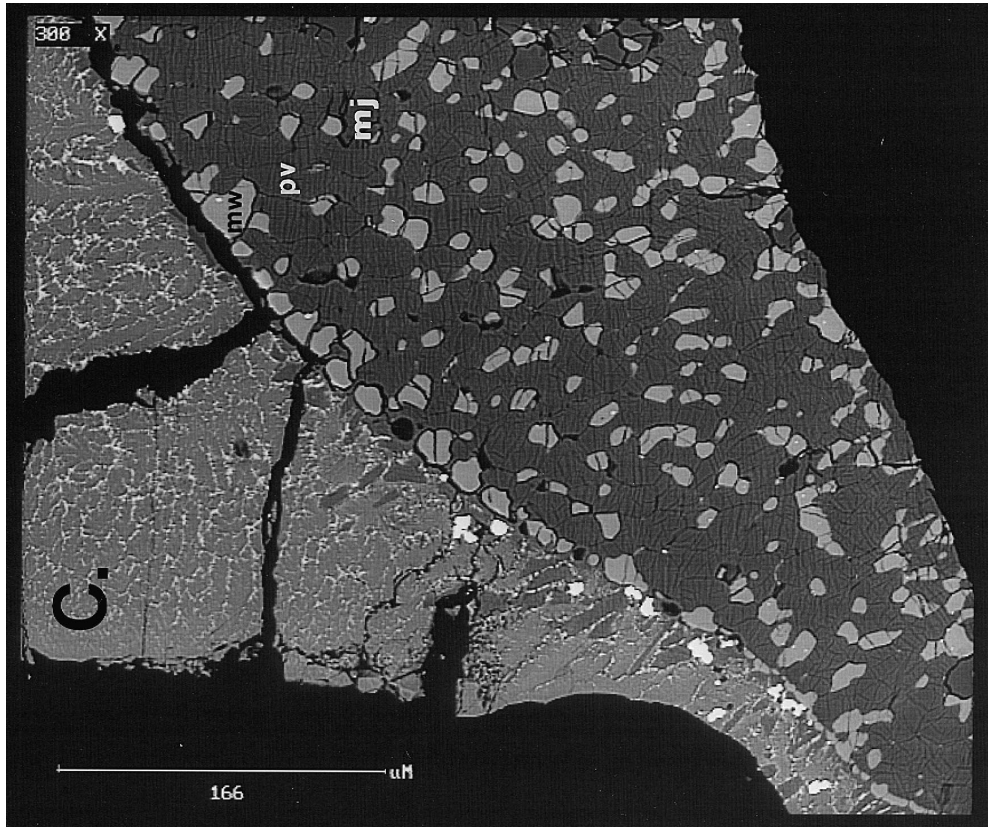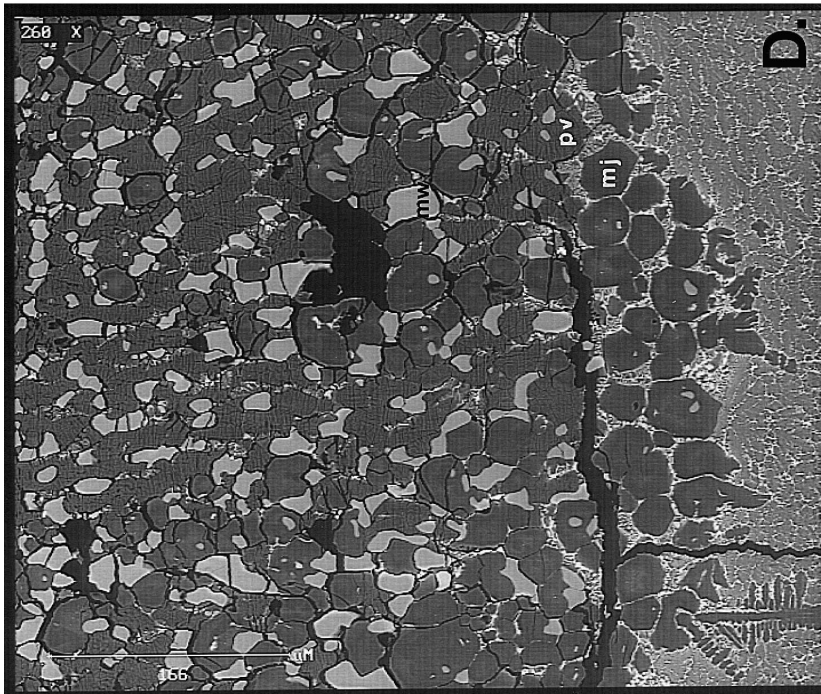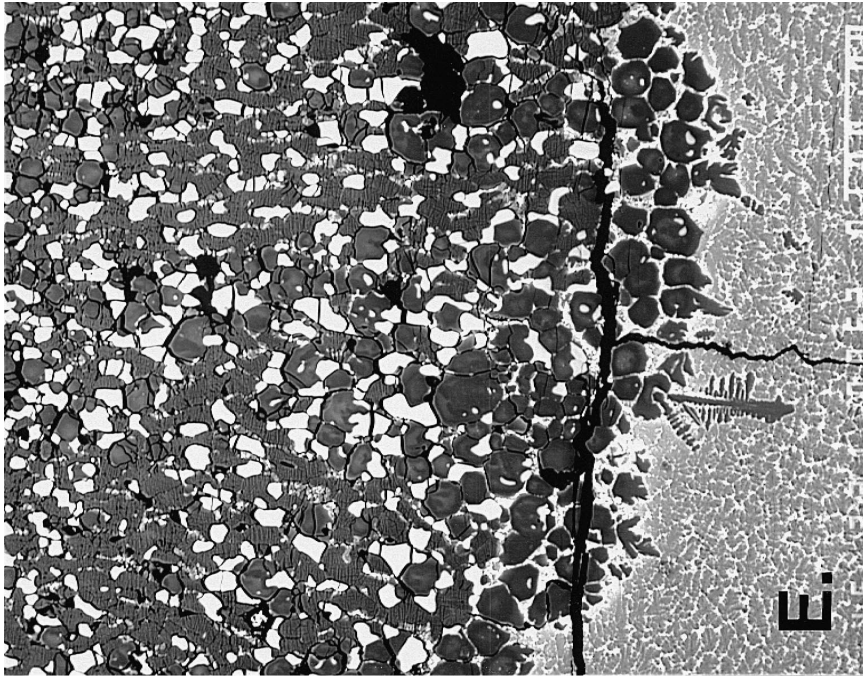
Figs. 5 and 6, the perovskite and garnet liquidus phases have strongly reduced ratios of Fe/Mg and Ca/Al, relative to the bulk composition. Fig. 6 shows that these ratios increase rapidly below the liquidus to become compatible with the bulk composition at the subsolidus. For liquidus magnesiowüstite in the 20–26 GPa range, the Mg/Fe ratios are similar to that of the bulk composition. The increasing Fe/Mg ratios from liquidus to solidus for all of the phases are shown by increasing BSE intensity in Fig. 4E and in Trønnes et al. (1992, Fig. 4). The strong and systematic variation in mineral composition within a few tens of micrometers away from the liquidus in experiments with large thermal gradients demonstrates the importance of obtaining reduced, or at least regular, thermal gradients in such experiments.

The coexisting majoritic garnet and perovskite at 26.2 GPa have relatively similar compositions. The liquidus garnet phase ranges from about 60% combined ''garnet'' components (i.e., pyrope, almandine and grossular) and 40% pyroxene components at 14.8 GPa to 43% garnet and 57% pyroxene at 24.3 GPa (Table 2). At 26.2 GPa, the coexisting perovskite contributes to a reduction of the pyroxene component in the liquidus garnet phase to about 50%.

Whereas all of the analyzed garnet phases have cation sums of 7.98–8.00 (normalized to 12 oxygen atoms), the perovskite at 26.2 GPa have cation sums of 8.11–8.16. Fitz Gerald and Ringwood (1991) synthesized and described the perovskite phase $Ca_{4.36}Al_{2.18}Si_{2.18}O_{12}$ $(Ca_2AlSiO_{5.5})$ with 8.72 cations per 12 oxygen atoms and speculated that this
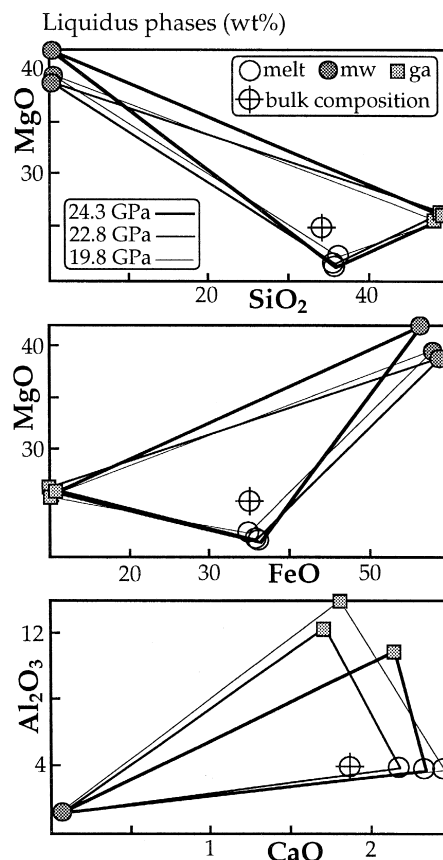

Fig. 5. Variation diagrams showing the coexisting liquidus phases in the experiments at 19.8, 22.8, and 24.3 GPa. The 2σ error bars are within (smaller than) the symbols for all of the elements and phases. Abbreviations are as in Fig. 3.

component could account for a considerable amount of Al (and Ca) in lower mantle perovskite. Based on

Fig. 4. Back-scattered electron (BSE) images of liquidus phase relations. (A) Run product no. 1337, 14.8 GPa. Scale bar is 250 μm. The estimated liquidus temperature is 1925°C, and the axial thermal gradient is 180–200°C/mm. Garnet is the liquidus phase (dark grains surrounded by quenched melt). The incoming phases away from the liquidus are magnesiowüstite (highest BSE-brightness) and $(Mg,Fe)_2SiO_4$ (intermediate brightness, bottom). Note that the true liquidus garnet crystals are larger (20–30 μm) than the garnet crystals that are included in magnesiowüstite (about 10 μm).

(B–E) Run product no. 1274, 26.2 GPa. (B) Overview of the run product. The central part is quenched liquid. The estimated liquidus temperature is 2180°C, and the axial thermal gradient is 200–300°C/mm. The shortest distance between the upper and lower liquidus interphases is about 700 μm. (C and D) Enlarged views of lower (C) and upper (D) liquidus interface. The scale bars are 166 μm. Note the gravitative accumulation of tiny fragments of Re metal (highest brightness) along the lower liquidus interface. The upper interface is irregular and broken with a zone of majoritic garnet (mj) grains next to the all-liquid area. Perovskite (pv) and magnesiowüstite (mw) grains appear to have sunk into the liquid from this zone. The lower interface is smooth and dominated by the densest minerals, mw and pv. Note the polysynthetic lamellae in the pv. (E) Approximately the same area as in (D), but with a more sensitive BSE intensity recording, showing the increasing BSE intensity (reflecting increasing Fe/Mg ratios) of all the phases away from the liquidus (upward direction).

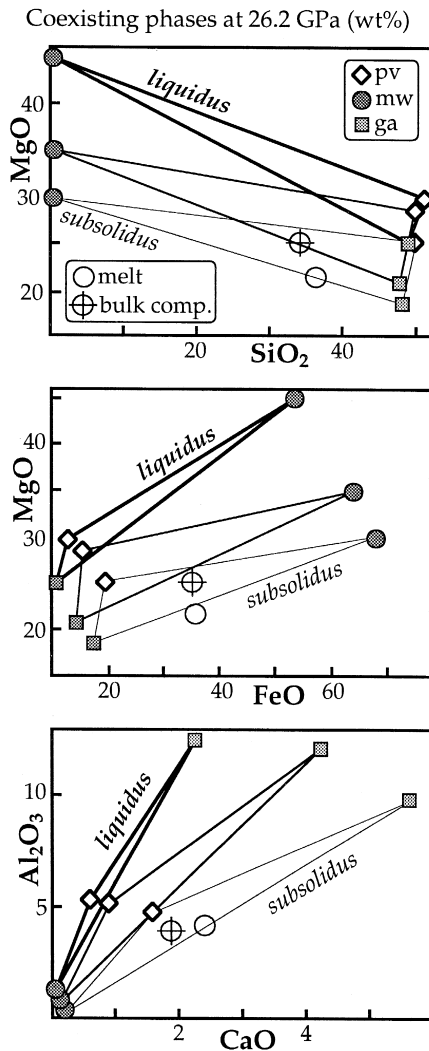Coexisting phases at 26.2 GPa (wt%)

Fig. 6. Variation diagrams showing the coexisting phases in the 26.2 GPa experiment. Bold lines connect the liquidus minerals, and thinner lines connect coexisting minerals 350 μm (labelled intermediate) and 700 μm (labelled subsolidus) away from the liquidus, respectively. The location of the solidus about 700 μm away from the liquidus is inferred from the coexisting mineral compositions that bracket the bulk system composition. The 2σ error bars are within the symbols for all of the elements and phases. Abbreviations are as in Fig. 3.

the cation sums of 8.11–8.16, the 26.2-GPa perovskites could contain up to 15–22 mol% of a $(Mg,Fe,Ca)_2AlSiO_{5.5}$ component. There are, however, minor amounts of ferric iron present in the experimental charges, due to the extraction of metal-

lic Fe for alloying with Re along the inner walls of the capsules. The studies of Wood and Rubie (1996), McCammon (1997), McCammon et al. (1997) and Wood (2000) indicate that perovskite has a strong affinity for ferric iron. If the entire cation excess of 0.11–0.16 in a formula normalized to 12 oxygen atoms is ascribed to the presence of ferric iron, the charge balance of a formula normalized to 8.00 cations requires an Fe^{3+}/Fe_{total} ratio of 0.35–0.50.

The mineral–melt partitioning coefficients for the Si/Mg, Fe/Mg, and Ca/Al ratios are shown as a function of pressure in Fig. 7. Except for the decreasing mw–melt partitioning of Fe/Mg with increasing pressure, there are only minor variations of the major element partitioning within the 15–26 GPa range. The $K_D(Fe/Mg)$ is slightly above unity at 15 GPa but considerably below unity above 20 GPa, indicating that mw fractionation in the lower part of the transition zone and the upper part of the lower mantle will increase the Fe/Mg ratio of the melt.
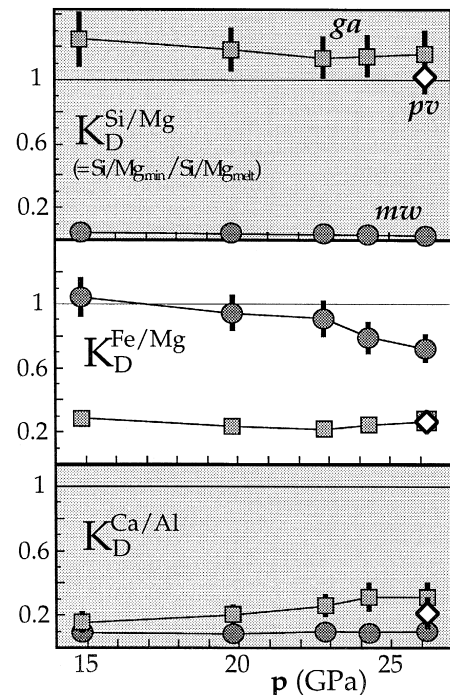

Fig. 7. Major element partitioning coefficients as a function of pressure. The propagated error bars (2σ level) are within the symbols except where indicated. Abbreviations are as in Fig. 3.

This applies, at an even greater extent, to the fractionation of garnet and perovskite. Fractionation of garnet and perovskite will increase the Ca/Al ratio of the melt.

4. Discussion

The mineral–melt partitioning relations indicate that fractional crystallization or partial melting in the transition zone and the upper part of the lower mantle would increase the Fe/Mg and Ca/Al ratios of the melt, even if a (Mg,Fe)O phase was predominant in the solid fraction. The observed Fe/Mg partitioning coefficients for mw are similar to those of Herzberg and Zhang (1996), in spite of the large difference in the bulk compositions. This study demonstrates that the composition of the liquidus MgFe-oxide is strictly a ferroan periclase in the 20–26 GPa range, even for the investigated very Fe-rich system. Whereas the K_D(Fe/Mg) for the mw-melt partitioning at 26 GPa is 0.7, Agee (1990, 1993) determined the corresponding K_D value to 3.6 in his melting study on the Allende meteorite. This large discrepancy may be a result of extreme thermal gradients and unstable temperature conditions in the experiments of Agee (1990). The analyzed compositions of the magnesiowüstite and melt in those experiments are, most likely, not representative of true liquidus compositions. Fig. 8 shows how the apparent partitioning coefficients for the Ca/Al and Fe/Mg ratios between the minerals perovskite, garnet and magnesiowüstite and the liquidus melt composition increases drastically towards the solidus. A similar increase is observed for the K_D(Si/Mg) for perovskite and garnet. Based on the results from the present study, contribution of accumulated magnesiowüstite to the segregation of the protocore (Agee 1990) is therefore unlikely.

The 26 GPa experiment indicates a relative density sequence of mw > pv > melt > mj for the investigated FeO-rich bulk Earth model composition. This density sequence is consistent with density–pressure relations of appropriate perovskite and magnesiowüstite compositions estimated by Agee (1998). At a pressure of 26 GPa, the observed liquidus magnesiowüstite (Mg# = Mg/(Mg + Fe) = 0.60) and per-
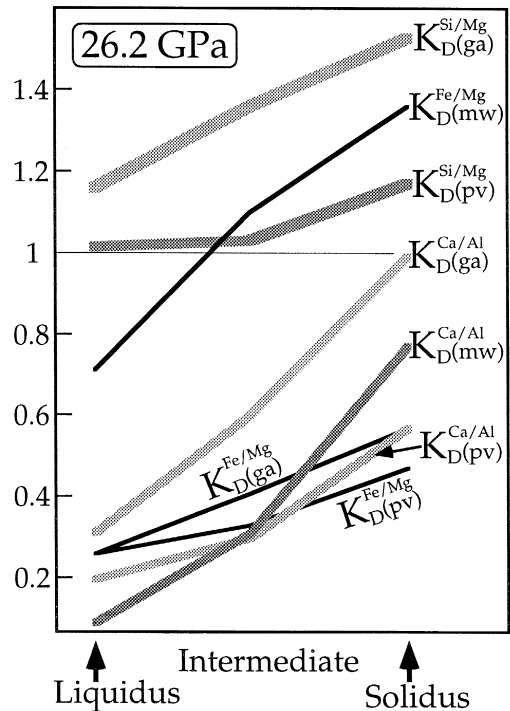

Fig. 8. Apparent partitioning coefficients at 26.2 GPa as a function of distance from the liquidus. The partitioning coefficients at distances of about 350 μm (intermediate position) and 700 μm (near the solidus) from the liquidus are calculated using the actual mineral compositions in combination with a constant quenched melt composition measured near the liquidus (Table 2). The interstitial melt pockets between the liquidus and solidus (Fig. 4D) are too small to be reliably measured.

ovskite (Mg# = 0.80) have expected densities of about 4.6 and 4.3 g/cm^3, respectively.

Majorite floating, combined with the sinking of magnesiowüstite and perovskite, can thus be expected in bulk compositions appropriate for the early, undifferentiated Earth. Agee and Walker (1988) suggested that magma ocean fractionation and sinking of perovskite to the lower mantle could contribute to the higher chondritic Mg/Si ratio of the upper mantle (e.g., Hart and Zindler, 1986; Allegre et al., 1995; McDonough and Sun, 1995). The K_D(Si/Mg) for pv–melt equilibrium in Fig. 7, however, is very close to unity (1.014), indicating that perovskite fractionation, at least for the investigated composition, would not contribute appreciably to a suprachondritic Mg/Si ratio of the upper mantle. Majoritic garnet flotation into the transition zone, in

combination with the sinking of perovskite and magnesiowüstite to the lower mantle, however, would clearly increase the Si/Mg and Mg/Fe ratios of the transition zone and lower the ratios of the lower mantle compared to an assumed chondritic starting composition. If magnesiowüstite would sink to a deeper level (e.g., core–mantle boundary) than perovskite, the result would be a relative enrichment of Fe and Mg in the deeper parts of the lower mantle and of Si (and Al and Ca) in the more shallow portions.

Whereas majoritic garnet and perovskite have similar Ca/Al ratios, the concentrations of these elements are more than twice as high in garnet as in perovskite. The effect of combined majorite floating into the transition zone and a comparable amount of pv sinking into the lower mantle would therefore be to increase the Al/Ca ratio and the Al and Ca concentrations in transition zone at the expense of the lower mantle.

The partitioning coefficient, $K_{pv/mw}^{Fe/Mg}$ for the Fe/Mg-distribution between coexisting perovskite and magnesiowüstite at 27 GPa is 0.37 and 0.34 at the liquidus and solidus, respectively. These values are in general agreement with the partitioning coefficients obtained by Kesson and Fitz Gerald (1991) and Katsura and Ito (1996). However, the uncertainties related to the strong tendency for ferric iron to enter the pv phase (McCammon, 1997; McCammon et al., 1997) will greatly influence the Fe/Mg partitioning relationships.

5. Conclusions

(1) In the investigated FeO-rich, ultramafic composition, olivine is the liquidus phase up to 12–14 GPa, followed by ga at higher pressures. Magnesiowüstite is the second crystallizing phase in the entire 10–24 GPa range, and at 26 GPa, MgFe-perovskite joins the liquidus phase assemblage. The melt appears to be nearly co-saturated in garnet, perovskite and magnesiowüstite at 26 GPa.

(2) The following relative density sequence is observed at 26 GPa: mw > pv > melt > majorite.

(3) The present experiments, characterized by large but regular and stable thermal gradients, demonstrate a strong and systematic variation in mineral composition within a few tens of micrometers away from the liquidus. The Fe/Mg and Ca/Al ratios in all minerals increase rapidly from liquidus to solidus. The derivation of correct mineral–melt partitioning coefficients are critically dependent on the ability of measuring the true liquidus compositions in such experiments. An ideal situation is the elimination or strong reduction of the thermal gradient (e.g., Walter, 1998). If the thermal gradient is regular and stable, however, it seems possible to obtain good liquidus phase analyses.

(4) The pyroxene component of the liquidus garnet phase increases from 40 to 57 mol% in the 15–24 GPa pressure range. At 26 GPa the pyroxene component in the garnet decreases to 50 mol%, because of the coexisting perovskite. A small cation excess in the perovskite formulas, normalized to a fixed number of oxygen atoms, indicates the presence of either some ferric iron (a maximum Fe^{3+}/Fe_{total} ratio of 0.50) or a $(Ca,Mg,Fe)_2 AlSiO_{5.5}$ component (maximum 22 mol%). Even for such an Fe-rich system, the liquidus FeMg-oxide is strictly a ferroan periclase in the 20–26 GPa pressure range.

(5) The quenched melt compositions are homogeneous throughout the all-melt parts of the experimental charges, and are only slightly enriched in Si, Ca and Fe, and depleted in Mg, relative to the bulk composition. The mineral–melt partitioning relations demonstrate that fractional crystallization or partial melting in the transition zone and upper part of the lower mantle will increase the Fe/Mg and Ca/Al ratios in the melt, relative to the bulk composition, even in an Fe-rich system with magnesiowüstite as an important residual phase. It is therefore unlikely that magnesiowüstite fractionation contributed significantly to the protocore segregation. Furthermore, perovskite fractionation by sinking into the lower mantle may not lead to increasing Mg/Si ratios of evolving melts. The combined fractionation of magnesiowüstite and perovskite produces melts with decreasing Mg/Si and Mg/Fe ratios.

References

Agee, C.B., 1990. A new look at differentiation of the Earth from melting experiments on the Allende meteorite. Nature 346, 834–837.

Agee, C.B., 1993. High-pressure melting of carbonaceous chondrite. J. Geophys. Res. 98, 5419–5426.

Agee, C.B., 1998. Crystal-liquid density inversions in terrestrial and lunar magmas. Phys. Earth Planet. Inter. 107, 63–74.

Agee, C.B., Li, J., Shannon, M.C., Circone, S., 1995. Pressure–temperature phase diagram for the Allende meteorite. J. Geophys. Res. 100, 17725–17740.

Agee, C.B., Walker, D., 1988. Mass balance and density constraints on early differentiation of chondritic mantle. Earth Planet. Sci. Lett. 90, 144–156.

Allegre, C.J., Poirier, J.-P., Humler, E., Hofmann, A.W., 1995. The chemical composition of the Earth. Earth Planet. Sci. Lett. 134, 515–526.

Anders, E., Grevesse, N., 1989. Abundances of the elements: meteoritic and solar. Geochim. Cosmochim. Acta 53, 197–214.

Fitz Gerald, J.D., Ringwood, A.E., 1991. High-pressure rhombohedral perovskite phase $Ca_2AlSiO_{5.5}$. Phys. Chem. Miner. 18, 40–46.

Green, T.H., 1995. Experimental studies of trace element partitioning applicable to igneous petrogenesis — Sedona 16 years later. Chem. Geol. 117, 1–36.

Hart, S.R., Zindler, G.A., 1986. In search of a bulk-Earth composition. Chem. Geol. 57, 247–267.

Herzberg, C.T., 1995. Generation of plume magmas through time: an experimental perspective. Chem. Geol. 126, 1–18.

Herzberg, C.T., Zhang, J., 1996. Melting experiments on anhydrous KLB-1: compositions of magmas in the upper mantle and transition zone. J. Geophys. Res. 101, 8271–8295.

Herzberg, C.T., Zhang, J., 1997. Melting experiments on komatiite analog compositions at 5 GPa. Am. Mineral. 82, 354–367.

Herzberg, C., O'Hara, M.J., 1998. Phase equilibrium constraints on the origin of basalts, picrites and komatiites. Earth-Sci. Rev. 44, 39–79.

Jones, J.H., 1995. Experimental trace element partitioning, Rock Physics and Phase Relations. A Handbook of Physical Constants. AGU Reference Shelf 3. Am. Geophys. Union, Washington.

Kato, T., Ohtani, E., Morishima, H., Yamazaki, D., Suzuki, A., Suto, M., Kubo, T., Kikegawa, T., Shimomura, O., 1995. In situ X-ray observation of high-pressure phase transition and thermal expansion of $MgSiO_3$ perovskite at 25 GPa by double-stage multianvil system. J. Geophys. Res. 100, 20475–20481.

Katsura, T., Ito, E., 1996. Determination of Fe–Mg partitioning between perovskite and magnesiowüstite. Geophys. Res. Lett. 23, 2005–2008.

Kesson, S.E., Fitz Gerald, J.D., 1991. Partitioning of MgO, FeO, NiO, MnO and Cr_2O_3 between magnesian silicate perovskite and magnesiowüstite: implications for the origin of inclusions in diamond and the composition of the lower mantle. Earth Planet. Sci. Lett. 111, 229–240.

McCammon, C., 1997. Perovskite as a possible sink of ferric iron in the lower mantle. Nature 387, 694–696.

McCammon, C., Hutchison, M., Harris, J., 1997. Ferric iron content of mineral inclusions in diamonds from Sao Luiz: a view into the lower mantle. Science 278, 434–436.

McDonough, W.F., Sun, S.-S., 1995. The composition of the Earth. Chem. Geol. 120, 223–253.

McFarlane, E.A., Drake, M.J., Herzberg, C.T., 1991. Magnesiowüstite/melt and majorite/melt partitioning and the early thermal history of the Earth. Proc. Lunar Planet. Sci. Conf. 22, 875–876.

O'Hara, M.J., 1968. The bearing of phase equilibria studies in synthetic and natural systems on the origin of basic and ultrabasic rocks. Earth-Sci. Rev. 4, 69–133.

Solomatov, V.S., Stevenson, D.J., 1993. Suspension in convective layers and style of differentiation of a terrestrial magma ocean. J. Geophys. Res. 98, 5375–5390.

Tonks, W.B., Melosh, H.J., 1993. Magma ocean formation due to giant impacts. J. Geophys. Res. 98, 5319–5333.

Trønnes, R.G., 1998. Melting relations and mineral–melt partitioning of an FeO-rich, bulk Earth model composition at 15–27 GPa. Origin of the Earth and Moon. LPI Contribution 957 Lunar Planet. Inst., Houston, pp. 47–48.

Trønnes, R.G., Canil, D., Wei, K., 1992. Element partitioning between silicate minerals and coexisting melts at pressures of 1–27 GPa, and implications for mantle evolution. Earth Planet. Sci. Lett. 111, 241–255.

Walter, M.J., 1998. Melting of garnet peridotite and the origin of komatiite and depleted lithosphere. J. Petrol. 39, 29–60.

Wetherill, G.W., 1990. Formation of the Earth. Annu. Rev. Earth Planet. Sci. 18, 205–256.

Wood, B.J., 2000. Phase transformations and partitioning relations in peridotite under lower mantle conditions. Earth Planet. Sci. Lett. 174, 341–351.

Wood, B.J., Rubie, D.C., 1996. The effect of alumina on phase transformations at the 660-kilometer discontinuity from Fe–Mg partitioning experiments. Science 273, 1522–1524.

Zhang, J., Herzberg, C., 1994. Melting experiments on anhydrous peridotite KLB-1 from 5.0 to 22.5 GPa. J. Geophys. Res. 99, 17729–17742.

Zhang, J., Liebermann, R.C., Gasparik, T., Herzberg, C.T., Fei, Y., 1994. Melting and subsolidus relations of SiO_2 at 9 to 14 GPa. J. Geophys. Res. 99, 17729–17742.